Minding the Gap between Plant and Bacterial Photosynthesis within a Self-Assembling Biohybrid Photosystem

Juntai Liu[1], Judith Mantell[1,2] and Michael R. Jones[1,*]

[1]*School of Biochemistry, Biomedical Sciences Building, University of Bristol, University Walk, Bristol BS8 1TD, United Kingdom.*

[2]*Wolfson Bioimaging Facility, Biomedical Sciences Building, University of Bristol, University Walk, Bristol BS8 1TD, United Kingdom.*

*Corresponding author. E-mail: m.r.jones@bristol.ac.uk

Abstract

Many strategies for meeting mankind's future energy demands through the exploitation of plentiful solar energy have been influenced by the efficient and sustainable processes of natural photosynthesis. A limitation affecting solar energy conversion based on photosynthetic proteins is the selective spectral coverage that is the consequence of their particular natural pigmentation. Here we demonstrate the bottom-up formation of semi-synthetic, polychromatic photosystems in mixtures of the chlorophyll-based LHCII major light harvesting complex from the oxygenic green plant *Arabidopsis thaliana*, the bacteriochlorophyll-based photochemical reaction centre (RC) from the anoxygenic purple bacterium *Rhodobacter sphaeroides* and synthetic quantum dots (QDs). Polyhistidine tag adaptation of LHCII and RC enabled predictable self-assembly of LHCII/RC/QD nanoconjugates, the thermodynamics of which could be accurately modelled and parameterised. The tri-component biohybrid photosystems displayed enhanced solar energy conversion *via* either direct chlorophyll-to-bacteriochlorophyll energy transfer or an indirect pathway enabled by the QD, with an overall energy transfer efficiency comparable to that seen in natural photosystems.

Keywords

biohybrid; self-assembly; quantum dots; photosynthesis; light harvesting; solar energy conversion

Greater and more diverse use of solar radiation could address mankind's growing needs for renewable energy and sustainable technologies.[1] Providing inspiration for achieving this in environmentally-benign ways, natural photosynthesis converts solar energy at a rate that is several times greater than our current energy demand.[2–4]

A feature of natural photosynthesis is that different organisms exploit different parts of the solar spectrum depending on their pigmentation.[5,6] Plants, algae and cyanobacteria contain chlorophyll (Chl) as their principal photosynthetic pigment (**Figure S1A**, Supporting Information) and exploit much of the visible spectrum.[3,5,7] In contrast, diverse anoxygenic photosynthetic bacteria utilise bacteriochlorophyll (BChl) (**Figure S1A**, Supporting Information) and occupy complementary light niches in the near-ultraviolet and near-infrared.[6–8] Strategies for overcoming the limitations of natural pigment palettes to expand solar energy conversion are central to the future development of photosynthetic systems[1,3,5,9–11] and are important considerations for biohybrid photoelectrochemical devices,[2,12–24] including BChl-based devices that have a relatively weak response to visible light.[14,25–34]

One option for producing photoproteins with a broader capacity for solar energy harvesting is to use synthetic dyes to target regions where natural absorbance is weak, such as the "green gap" of chlorophyll-based photosystems[35,36] or the "red gap" of bacteriochlorophyll-based photosystems.[37,38] An alternative is to use more photostable fluorescent nanoparticles to act as synthetic light harvesting[39,40] or reaction center components for solar energy conversion.[41]

Inspired by the diversity of light harvesting materials in natural photosynthesis, here we report a semi-synthetic photosystem comprising three, normally-foreign, components that display complementary spectral coverage (**Figure 1A**), namely the reaction centre (RC) from the BChl-containing bacterium *Rhodobacter* (*Rba). sphaeroides* (**Figure S1B**, Supporting Information), the LHCII light harvesting complex from *Arabidopsis* (*A*)*. thaliana* (**Figure S1C**, Supporting Information) and cadmium-telluride quantum dots (QDs). The strong absorbance of the RC in the near-UV (300-400 nm) and near-IR (700 ~ 900 nm) originates from its BChl pigments, which have a differently-shaped π-conjugated system to that of the Chl pigments of LHCII (**Figure S1A**, Supporting Information). Chl has complementary strong absorbance in the red and blue regions of the visible spectrum (400-700 nm, **Figure 1A**), with spectral overlap between LHCII emission and RC absorbance between ~650 and ~800 nm. CdTe QDs have broad absorbance across the visible and UV region that increases in intensity with decreasing wavelength (**Figure 1A**). The QDs used in the present work were selected to have an emission band that overlapped with RC absorbance between 650 nm and 850 nm. The system was therefore designed such that energy captured by the Chls of the green plant LHCII could be transferred to the BChl charge separation

system of the purple bacterial RC either directly or *via* an energy conduit provided by the 750 nm-emitting QDs (**Figure 1A,B**).[42] Although these two proteins from different kingdoms of life have no natural propensity to associate or engage in strong energetic coupling, it was found that by adaptation with suitable poly-histidine tags they could be induced to self-assemble with QDs into predictable tricomponent nanoconjugates. This resulted in tuneable energy transfer (ET) that exhibited an efficiency comparable to that seen in natural photosystems with evolved components. This adaptable biohybrid nanoconjugate also reflects strategies within natural photosystems that ensure high efficiency, and plasticity to changes in environmental conditions.[9,10]

Results and Discussion

Assembly and characterisation of di-component LHCII/QD nanoconjugates.

Di-component nanoconjugates assembled between LHCII and the water-soluble CdTe QDs were first characterised. A gene encoding LHCII was modified to create a C-terminal deca-histidine tag (**Figure 1B** and **Figure S2A**, Supporting Information) and the resulting monomeric $LHCII_H$ holoprotein was refolded from apoprotein expressed in *Escherichia* (*E.*) *coli* and purified pigments[43] (see Section 1 of Supporting Information). Analysis by ultracentrifugation on two-step sucrose density gradients (see Methods/Experimental) showed that this His_{10}-tag modification produced approximately 90% binding to QDs (**Figure 1D**) in contrast to hardly any binding by native LHCII purified from spinach (**Figure 1C**). This paralleled previously-reported strong and specific binding of His_{10}-tag-modified RCs (dubbed RC_H) to the same QDs[39] (**Figure 1E**) and a 1:1 mixture of $LHCII_H$ and RC_H also bound strongly to QDs (**Figure 1F**). Modification of the same LHCII with a hexa-histidine tag produced only weak binding to the QDs (~ 30%; **Figure S2B**, Supporting Information).

As previously demonstrated for RC_H,[39] a model employing finite, multiple, independent binding sites[44,45] (**Figure 2A**) was effective in describing sucrose density gradient data on the binding of $LHCII_H$ to QDs over a range of supplied $LHCII_H$:QD ratios (**Figure S3A,B**, Supporting Information). Details of this model are given in Section 2 of Supporting Information (**Eqs. S1-S5**, Supporting Information). The best fit of the model to experimentally determined average binding ratios (**Figure 2B**, Supporting Information) produced a micro-kinetic constant (k_{micro}) of 7.19 μM^{-1} and a maximum permitted binding number ($\bar{n}$) of 17. Using **Eq. S2 (**Supporting Information) a K_d of 8.2 nM was obtained for the first $LHCII_H$ to bind to a QD. This was very close to an equivalent value of 8.1 nM obtained in a recent analysis of the binding of RC_H complexes to the same QDs.[39] The model showed that the protein to QD stoichiometry followed a Poisson distribution at low

saturation levels[46] but overall followed a binomial distribution due to a finite number of binding sites.[44]

The nature of this strong interface between the protein His_{10}-tag and the CdTe QD is considered to be a coordinate interaction in which the histidine side chains chelate surface cadmium (**Figure S4A**, Supporting Information), since binding (as assessed from energy transfer) could be reversed with free histidine or imidazole but not with equivalent concentrations of NaCl (**Figure S4B**, Supporting Information).

Titration of QDs with increasing $LHCII_H$ produced a decrease in $LHCII_H$ fluorescence relative to concentration-matched $LHCII_H$-only controls (**Figure 2C,** solid *versus* dashed green) and a corresponding increase in QD fluorescence (**Figure 2C,** solid brown). This indicated ET, presumably *via* a Förster resonance mechanism (FRET) at this separation distance (**Figure 2D**). ET efficiencies were estimated as described in Section 3 of Supporting Information (**Eqs. S6-S7**, Supporting Information) by combining these data on $LHCII_H$ and QD fluorescence (**Figure 2C**) with the data above on the thermodynamics of $LHCII_H$/QD conjugation. An estimate of mean single donor to single acceptor ET efficiency based on quenching of $LHCII_H$ fluorescence ($E_{DA(LHCII)}$) of 37.1 ± 1.7% agreed well with a mean value of 36.1 ± 2.0% estimated from enhancement of QD fluorescence ($E_{DA(QD)}$), with no dependence on the $LHCII_H$:QD ratio (**Figure 2E**). This agreement supported the conclusion that the ET mechanism was FRET and indicated that the functionality of $LHCII_H$ was not affected by binding to the QD. As detailed in Section 3 of Supporting Information (**Eqs. S8-S9**, Supporting Information), the FRET distance R was estimated to be 7.4 ± 0.1 nm, giving a diameter of 19.8 ± 0.2 nm for an $LHCII_H$/QD nanoconjugate based on the assumption that this FRET distance is from the centre of a QD to the centre of a bound $LHCII_H$. The estimated E_{DA} for LHCII→QD energy transfer of 36-37% was somewhat lower than an equivalent E_{DA} of ~53% for the transfer of energy from the same QDs to RC_H reported previously (see Section 3 of Supporting Information for more details).[39]

Assembly and architecture of tri-component LHCII/RC/QD nanoconjugates.

As illustrated in **Figure 1F**, tri-component nanoconjugates were formed when $LHCII_H$ and QDs were mixed with His_{10}-tagged RC_H complexes (see Section 4 of Supporting Information). Fifteen types of nanoconjugate were separated from unbound protein on sucrose density gradients (**Figure S5A**, Supporting Information). These were formed in mixtures with three different $LHCII_H$:RC_H ratios, with each at five different total protein to QD molar ratios (termed "total-protein:QD" ratio). Importantly, spectroscopic analysis of the nanoconjugate band showed that its content of bound $LHCII_H$ and RC_H was determined by the supplied solution concentrations

in the initial mix up to a total-protein:QD ratio of 10 (**Figure S5B**, Supporting Information). Above this ratio the composition biased toward RC_H, an effect likely attributable to subtle differences between the two proteins, particularly with regard to their size and the longer linker connecting the His_{10}-tag to the RC. The longer linker could mean that the RC_H has more freedom to move than $LHCII_H$ when tethered to the QD surface and is therefore better able to tolerate, or adjust to, competition for binding from $LHCII_H$.

Transmission electron microscopy (TEM) provided direct visualization of nanoconjugate formation, the addition of QDs triggering reorganisation of monodispersed small proteins (<10 nm) into much larger protein/QD nanoconjugates (**Figure S6A**, Supporting Information). **Figure 3A** shows the type of multi-lobed object that resulted from binding of multiple $LHCII_H$ to a QD (**Figure 3B**). Due to the lack of defined binding sites on the QD surface, and population heterogeneity in the final configuration/architecture of the protein/QD conjugates, the detailed morphology observed by TEM was variable. Therefore, the individual object shown in **Figure 3A** should be taken as an example rather than definitive of the population. Image analysis (**Figure S6B-C**, Supporting Information) produced estimates of nanoconjugate diameter that could be fitted with a lognormal distribution with a mode at 19.3 ± 1.0 nm (**Figure 3C**), consistent with the diameter of 19.8 ± 0.2 nm deduced from FRET analysis (see above).

Tri-component $LHCII_H/RC_H$/QD nanoconjugates formed in an equimolar mixture of $LHCII_H$ and RC_H were also examined by TEM (**Figure 3D-E**), and image analysis (**Figure S6D-E**, Supporting Information) produced a higher mode diameter of 21.5 ± 1.0 nm (**Figure 3F**). This was consistent with RC_H being larger than $LHCII_H$, and the diameter was very close to a value of 21.4 ± 1.0 nm reported recently from an equivalent analysis of RC_H/QD nanoconjugates.[39] A similar profile (mode diameter of 21.1 ± 1.0 nm) was also obtained for $LHCII_H/XylE_H$/QD nanoconjugates (**Figure 3G-I**) in which the protein $XylE_H$ was used as a photo-inactive "dummy" membrane protein of a similar size to RC_H and with the same His_{10}-tag. This suggested that the diameter of a tri-component nanoconjugate was dictated by the larger protein.

Chl to BChl ET in tri-component nanoconjugates.

ET to the non-emissive RC_H was measured through the bleaching of the 870 nm absorbance band of the primary electron donor BChls that occurs as a consequence of charge separation (see legend to **Figure S1B**, Supporting Information). Illumination was centred at 650 nm where RC absorbance is very low compared to that of QDs and, in particular, $LHCII_H$ (**Fig S7A**, Supporting Information). The kinetics of ΔA_{870} (**Figure S8**, Supporting Information) were fitted with an interconversion reaction (**Eq. 1** in Methods/Experimental) and rates of bleaching

during 7 s illumination and recovery during a subsequent dark period determined (**Figure S7B-C**, Supporting Information). Considering the compared fits in **Figure 4A**, photochemistry in a mixture of QDs, $LHCII_H$ and RC_H was strongly enhanced relative to other combinations, including concentration-matched controls with wild-type RCs without a His-tag (denoted "RC_{WT}" in **Figure 4A**). This showed that significant ET could be switched on only when both proteins were modified with a His_{10}-tag and were in the presence of QDs. The amount of RC photochemistry depended on the $LHCII_H$:RC_H ratio in the mix used to form the nanoconjugate (**Figure 4B**), increasing with more $LHCII_H$ per RC_H as the size of the $LHCII_H$/QD antenna servicing each RC_H increased. The rate of dark charge recombination remained invariant (**Figure S7C**, Supporting Information), indicating that the reversibility of RC photochemistry was unaffected by association with the QD.

$LHCII_H \rightarrow RC_H$ ET was also indicated by a quenching of $LHCII_H$ fluorescence in $LHCII_H$/RC_H/QD nanoconjugates that was not seen when the same concentrations of $LHCII_H$ and RC_H were mixed in the absence of QDs. The extent of this quenching did not depend on the order of mixing of components (**Figure S9A**, Supporting Information) indicating that the state being measured was at equilibrium.

Chl to BChl ET could in principle occur either by a direct route or an indirect route mediated by the QD hub (**Figure 4C**). The relative contributions of the two routes were investigated by measuring $LHCII_H$ and QD fluorescence at four total-protein:QD ratios in samples with a 1:1 ratio of $LHCII_H$ to RC_H or RC_{WT} (**Figure 4D**). Measured fluorescence was normalised to that from the same concentration of $LHCII_H$ or QD in sets of single component controls. Normalised fluorescence from $LHCII_H$ in RC_{WT}+$LHCII_H$/QD samples ($R_{Di,LHCII}$) did not vary with total-protein:QD ratio showing there was no reabsorption by (unattached) RCs (**Figure 4D**, green dash). In contrast, $LHCII_H$ fluorescence in compositionally matched $LHCII_H$/RC_H/QD samples ($R_{Tri,LHCII}$) declined as the total-protein:QD ratio increased (**Figure 4D**, green solid). The difference between these trends, $LHCII_H$ quenching seen only when RCs were bound to QDs, provided a means to estimate direct $LHCII_H \rightarrow RC_H$ ET (**Figure 4C**). This decline was not seen when RC_H was replaced with unpigmented $XylE_H$ (**Figure S9B**, Supporting Information) demonstrating that it was not the result of the attachment a second protein *per se* but was specific to RC_H acting as an energy sink.

QD fluorescence ($R_{Tri,QD}$) also declined gradually in $LHCII_H$/RC_H/QD samples as the result of $QD \rightarrow RC_H$ ET (**Figure 4D**, magenta solid), whilst in the equivalent RC_{WT} + $LHCII_H$/QD controls the QD fluorescence ($R_{Di,QD}$) increased with increasing total-protein:QD ratio (**Figure 4D**, magenta dash) as the consequence of increasing $LHCII_H \rightarrow QD$ energy flow. This offered a means to estimate indirect ET. Similar trends in $LHCII_H$ and QD fluorescence were seen in experiments with 2:1 and 1:2 mixes of $LHCII_H$ and either RC_H or RC_{WT} (**Figure S10A-B**, Supporting Information).

Assembly and compositions of tri-component nanoconjugates.

For a mixture of RC_H and $LHCII_H$ the kinetics of nanoconjugate assembly can be viewed as a competitive process in which each protein binds to free "sites" on a QD that are not occluded by already-bound protein. For the tri-component system there are four coordinates along which a nanoconjugate associated with multiple copies of RC_H and $LHCII_H$ could migrate from a defined state (**Figure 5A**). Nanoconjugates formed in protein mixtures with fifteen different total-protein:QD and $LHCII_H$:RC_H ratios were modelled as described in Methods/Experimental using the reaction schemes depicted by **Eqs. 2**-**3**. Two additional parameters were included in the model to account for preferential binding of RC_H at high total-protein:QD ratios (see above and **Figure S5B**, Supporting Information). Parameter α accounted for the shielding effect of already bound $LHCII_H$ on binding of an additional RC_H, whereas parameter β accounted for the reverse influence.

The model summarised in **Eqs. 2-9** in Methods/Experimental was used to describe experimental data on average RC_H:QD and $LHCII_H$:QD stoichiometries in nanoconjugates, derived from spectroscopic analysis of sucrose density gradients (**Figure S5B**, Supporting Information). The best fit of the model (black bars) to the data for RC_H (purple/pink bars) and $LHCII_H$ (green/cyan bars) was achieved with $\alpha = 0.63$ and $\beta = 0.78$ (**Figure 5B**). That both these parameters had a value less than one suggested that each of $LHCII_H$ and RC_H had a smaller influence on binding of the partner protein than on themselves, and the lower value for α was consistent with RC_H being more competitive for binding than $LHCII_H$ despite their very similar micro kinetic constants.

Distributions around the average compositions of tri-component nanoconjugates were modelled as described in Methods/Experimental. In an example result for nanoconjugates formed from an initial 5:5:1 $LHCII_H$:RC_H:QD mix, the most favoured compositions were close to that supplied (**Figure 5C**). Distributions for five other total-protein:QD ratios with equimolar $LHCII_H$ and RC_H are shown in **Figure S11** of Supporting Information. Modelling across a broader range of total-protein:QD ratios (1.25 to 128) and solution $LHCII_H$:RC_H ratios (0.3 to 2.2) showed that binding of RC_H was relatively insensitive to the presence of $LHCII_H$ at high total-protein:QD ratios **(Figure 5D)**. However, when this ratio was below approximately 13 the bound fractions were directly determined by the ratio of the two proteins in solution (**Figure 5D**), in agreement with experimental observations (**Figure S5B**, Supporting Information), since competition was small as the number of occupied "binding-sites" was below saturation.

An insight from the modelling of conjugation was that, in a mixture of composition $LHCII_H$:RC_H:QD = 5:5:8, only a very small proportion of QDs had both a $LHCII_H$ and a RC_H bound, and thus most were incapable of either direct or indirect $LHCII_H \rightarrow RC_H$ ET (**Figure 6A** – highlighted in greyscale). This was consistent with fluorescence titration experiments where, for samples with this 5:5:8 ratio (left-most in **Figure 4D**), $LHCII_H$ fluorescence was the same in mixtures with (bound) RC_H or (unbound) RC_{WT}. As the $LHCII_H$:RC_H:QD ratio rose to 5:5:1, the nanoconjugate population distribution migrated away from the ET-inactive zone (**Figure 6B**, and see **Figure S12E-H**, Supporting Information for other cases). Again, this was consistent with the progressive quenching of $LHCII_H$ fluorescence in samples with QDs and RC_H but not in samples with QDs and RC_{WT} (**Figure 4D**). A slight increase of the ET-inactive sub-population, especially at low total-protein:QD ratios, was seen when $LHCII_{:H}$:RC_H was biased from unity (**Figure S12A-D,I-L**, Supporting Information).

Estimation of direct and indirect energy transfer.

Efficiencies of direct (E_{Direct}) and indirect ($E_{Indirect}$) FRET in tri-component nanoconjugates were calculated combining these data on population heterogeneity with the data above on $LHCII_H$ and QD fluorescence (see Methods/Experimental and Section 5 of Supporting Information). E_{Direct} was estimated from a comparison of $LHCII_H$ fluorescence in the tri-component and di-component nanoconjugates (see **Eq. 10**). $E_{Indirect}$ was estimated using **Eq. 11** from the effective efficiencies of $LHCII_H \rightarrow$QD ET ($E'_{LHCIItoQD}$) and QD$\rightarrow RC_H$ ET (E'_{QDtoRC}) that considered only those nanoconjugates with at least one bound $LHCII_H$ and RC_H.

Variations of E_{Direct} and $E_{Indirect}$ with total-protein:QD ratio at an $LHCII_H$:RC_H equal to one are compared in **Figure 6C**. Both were negligible at $LHCII_H$ (RC_H):QD <1 but rose markedly up to ten total-proteins per QD. Indirect ET switched on before the direct pathway since energy flow mediated by the QD did not require apposition of an $LHCII_H$ and RC_H, while E_{Direct} outstripped $E_{Indirect}$ at high total-protein:QD ratios because of increasing protein crowding. Similar trends were obtained for $LHCII_H$:RC_H ratios other than one (**Figure S13**, Supporting Information).

For any given total-protein:QD ratio, the relative contributions of E_{Direct} and $E_{Indirect}$ to overall efficiency ($E_{Overall}$) were sensitive to the $LHCII_H$:RC_H ratio (**Figure 6D**), with $E_{Overall}$ seeming to plateau at a $LHCII_H$:RC_H ratio equal to one (**Figure 6D**, maroon). This can be envisaged as a situation where, on average, every bound $LHCII_H$ was adjacent to multiple RC_H and *vice versa*, producing an E_{Direct} that was about double that of $E_{Indirect}$. When the $LHCII_H$:RC_H ratio was increased to 2 (**Figure 6D**, green), a decrease in $E_{Overall}$ was obtained due to a drop in E_{Direct}. This could be due to a sub-fraction of the major $LHCII_H$ population not being sufficiently close to a

member of the minor RC_H population for effective direct FRET to take place, causing a waste of absorbed energy. However, for every RC_H there were more $LHCII_H$ within FRET distance and therefore enhanced P870 photobleaching was observed (**Figure 4B**, green). In contrast, when RC_H was supplied in a 2:1 ratio over $LHCII_H$ the ET efficiencies did not deviate substantially from those seen with a 1:1 mix (**Figure 6D**, purple). In this case, on average, each $LHCII_H$ will be adjacent to multiple RC_H, enabling efficient ET. However, this scenario also has the possibility of a fraction of RC_H that are not adjacent to an $LHCII_H$ and so do not receive energy efficiently, accounting for the observed lower level of P870 photobleaching (**Figure 4B**, purple).

Modular design of a photosystem with a generalised protein-QD interface.

In addition to their enormous utility for protein purification, polyhistidine tags are valuable for the fabrication of nanoscale biohybrid assemblies due to their affinity for a range of metallic materials.[39,47,48] A key finding underpinning the present work was that a deca-histidine tag could be used as a standardized universal interface between two different integral membrane photoproteins and a CdTe QD assembly hub. This enabled predictable self-assembly of tri-component energy-converting conjugates with different compositions by simply manipulating the protein composition of the initial mix, building complexity onto our previous work on bi-component RC/QD conjugates.[39,47,48]

These findings with engineered monomeric LHCII proteins provide an interesting contrast with previous work by Werwie *et al.* on the interaction of His-tagged pea LHCII with water-soluble QDs.[41,48] The recombinant LHCII complexes used in their work also had eleven amino acids removed from the N-terminus, with a His_6 tag placed at either the N- or C-terminus, but in contrast to the present work were induced to trimerize by refolding in the presence of phosphatidylglycerol. Their synthesised CdTe/CdSe/ZnS core-core-shell QDs also had a different anionic capping layer (3-mercaptopropionic acid *versus* dihydrolipoic acid) and a different surface material (ZnS) to the commercial CdTe QDs used here. Unlike in the present study where binding mediated by a His_6-tag was very weak, Werwie and co-workers were able to achieve strong binding with their modified LHCII, a finding they attributed to a combined effect of the His_6-tag and a positively charged domain at the N-terminus of the protein. Another factor affecting binding will have been their use of trimeric LHCII with three copies of the positive domain and His_6 tag, and differences in the surface chemistry of the different QDs. Strong binding of trimeric LHCII to the CdTe/CdSe/ZnS QDs was limited to one per QD, with indications from spectroscopic measurements of a second, weakly bound trimer[42]. In good agreement with our findings, fluorescence from LHCII trimers was quenched by bound QDs indicating FRET between the two.[41,48]

In the similar content, we have reported previously that the purple bacterial light harvesting 1 (LH1) complexes lacking a His-tag can associate with the same QDs as used in the present study, although when combined with a His-tagged RC in a RC-LH1 complex the binding affinity was further boosted.[49] In contrast, in the present work the binding of isolated RCs or LHCII monomers to the QD hub seemed to be dictated solely by the deca-histidine tag, with no influence of the attached protein. The choice of monomeric $LHCII_H$ complexes rather than LHCII trimers enabled the binding of multiple copies to each QD and the self-assembly of an intermingled $LHCII_H$ donor/RC_H acceptor protein shell. In modelling the assembly process a number of simplifying assumptions had to be made concerning the nature of the QD component, in particular, and the details of the binding of the proteins to the QD surface. This included use of an average weight and diameter for the 750 nm emitting QDs (in reality these are distributed around these averages), and assumptions over uniformity in the shape of the QDs and their capacity to bind protein. These assumptions will have affected parameters such as absolute protein:QD ratios, which should therefore be taken as estimates of population averages.

Adoption of natural light harvesting strategies in the design of a biohybrid photosystem.

In the tri-component conjugates, ET from $LHCII_H$ proteins to RC_H complexes took place by both a direct route and an indirect route mediated by the QD hub. The onset of indirect ET was earlier than for the direct route (**Figure 6C,** pink and **Figure 6E** brown trace/pink region) as it required co-binding of only a single $LHCII_H$ and a single RC_H to a QD. However, as the protein shell became more crowded the contribution of indirect route flattened off such that it made a minor contribution at the highest ratio of total-protein:QD. We attribute this to the less efficient LHCII to QD ET forming a bottleneck in the indirect route (see **Figure S13A**, Supporting Information), and this could be targeted for improvement in the future. The plateauing of the indirect route with increasing total-protein:QD ratio is considered to be the consequence of competition for the $LHCII_H$ exciton reservoir by direct ET (**Eq. S14**, Supporting Information and discussed in more detail in Section 5 of Supporting Information).

In addition to their own energy harvesting role, and their function as an assembly hub, the QDs provided an indirect route for ET from LHCII to the RC. In this scenario the QDs played a role reminiscent of that fulfilled by minor light harvesting components such as CP26 and CP29 in green plant Photosystem II (PSII) supracomplexes[50–52] which fill the gap between the major LHCII antennas and the PSII core[53] and are vital to the overall high efficiency of energy trapping (estimated at ~83%).[54] In the present case the additional energy bridge provided by the QD

produced an $E_{Overall}$ of as high as 58% (± 6%) when the total-protein:QD ratio was 10:1 (**Figure 6D**), with a quarter of the overall efficiency stemming from the indirect route (**Figure 6C**).

The photochemistry of each RC_H energy trap increased as the ratio of $LHCII_H$:RC_H increased (**Figure 4B**) due to more absorbance cross-section being provided in the red spectral region around 650 nm used for excitation, whereas the ET efficiency dropped off when $LHCII_H$ outnumbered the RC_H energy traps (**Figure 6D**). This latter observation has interesting parallels with natural systems which also display decreases in ET efficiency with increasing antenna size, albeit at much higher numbers of antenna complexes per RC.[55,56] The difference from natural systems is that the optimum configuration of the conjugates appeared to be around one LHCII per RC, due to the transfer of energy only occurring between adjacent LHCIIs and RCs. In both green plants and purple bacteria the evolution of very efficient energy conduits enables multi-step ET from distal light harvesting complexes, thereof organisms can benefit from an investment in light harvesting capacity.[8,51,55,57] This brings a number of advantages, including the option to modulate the efficiency of energy supply by adjusting the size of the antenna and its connectivity to the RCs for light acclimation.[9,10] Modulation along similar lines was also possible in the present case by varying the ratio of supplied LHCII and RC, predictability coming from the similar binding affinities stemming from the common mechanism for binding through the His_{10}-tag. However, in comparison to natural systems, a very small antenna per RC was needed for optimal performance.

Significant increases in the relative efficiency of direct FRET as the ratio of total-protein:QD increased (**Figure 6C**, green and **Figure 6E,** green trace/green region) are attributed to a reduction in RC_H-$LHCII_H$ separation as the QD surface became more crowded, bringing more donor-acceptor pairs within the FRET radius. Control of the separation of participants in the energy flow could also be a target for the future development of more advanced systems able to respond to environmental changes such as signal molecules or light intensity, mimicking the strategy used in plants such as balancing energy partition between Photosystem I (PSI) and PSII by varying their proximity to LHCII.[58]

Finally, the primary motivation behind our assembly of a photoactive conjugate from complementary components is to explore the expansion of solar energy harvesting by the purple bacterial RC. Although these RCs are tractable and relatively robust, a drawback is their relatively weak response to visible light, particularly in the red spectral region where Chl absorbance is strong. The conjugates described above therefore offer one route to the development of semi-synthetic photosynthetic systems that display enhanced solar energy harvesting, with a Chl-based antenna passing energy downhill to a BChl-based transducer.

Although a second potential drawback of such a system is that charge separation among the BChls of the purple bacterial RC produces less oxidising or reducing potentials than those generated by the Chls of PSII and PSI, respectively, this is offset by the relative stability and simplicity of purple bacterial photoproteins and the relative ease with which they can be adapted through genetic modification. Thus, although not suited to a high energy application such as water splitting, a variety of potential applications have been discussed for devices based on purple bacterial photoproteins ranging from biosensing and touch sensing to charge storage.[14,34,59] The enhancement of the solar energy harvesting capacities of such protein-based devices through the use of multicomponent photosystems is likely to further broaden their applicability for processes that do not require highly oxidising or reducing potentials.

Conclusions

This work demonstrates the self-assembly of biohybrid, polychromatic photosystem nanoconjugates comprising the purple bacterial RC, the major plant LHCII antenna and synthetic QDs that display enhanced solar energy conversion. In addition to acting as a hub for self-assembly of this bottom-up redesigned photosystem, the QD component bridged an energy gap between the plant and bacterial photosystems. The combination of the resulting direct and indirect FRET pathways produced an efficient flow of energy from the LHCII solar harvesters to the RC photochemical traps. Both the overall efficiency and flux down the two pathways could be tuned in a predictable manner by simply varying the stoichiometry of $LHCII_H$, RC_H and QD in the mix used for self-assembly. The demonstrated systematic understanding of the thermodynamics and ET characteristics of these LHCII/RC/QD photosystems provides insight into the interplay between nanomaterials and components from biological photosystems.

Methods/Experimental

Photosystem components. Water-soluble Cd/Te QDs coated with 3-mercaptopropionic acid with an emission maximum at 750 ± 5 nm and an average molecular weight of 550 KDa were purchased from PlasmaChem GmbH. The relatively narrow and symmetrical emission (**Figure S14**, Supporting Information) was indicative of a narrow size distribution (centred at 6.5 nm) and good monodispersity. Details of the engineering, refolding and purification of LHCII is given in Section 1 of Supporting Information. Details of the engineering and purification of RCs is given in Section 4 of Supporting Information.

Separation and analysis of nanoconjugates. Two step discontinuous sucrose density gradients were used to separate QDs or protein/QD nanoconjugates from free proteins. Gradients were formed from equal volumes of 25 % and 60 % (w/v) sucrose in 20 mM tris(hydroxymethyl)aminomethane (Tris, pH 8.0) /0.04 % *n*-dodecyl-β-D-maltopyranoside (Tris/DDM) in 12 mL ultracentrifuge tubes. Samples were premixed with 2 mM Tris(2-carboxyethyl)-phosphine. A standard loading of a 2.5 μM protein solution was used with a varying concentration of QDs. Loaded tubes were centrifuged at 38,000 rpm for 4 hours at 19^{o}C in a swing-out rotor (TH-641, Sorvall) and stored at 4^{o}C. Gradients were deconstructed into 11 fractions. The first eight from the bottom and middle of the gradient corresponded to QDs or nanoconjugates. Fractions 9-11 from the top of the gradient corresponded to unbound proteins. The integrity and concentration of protein and QD in each fraction was assessed by absorbance spectroscopy, with deconvolution to obtain spectra of individual components.

TEM and image analysis. Negative stain TEM was carried out on nanoconjugates formed from mixtures in which there was a 10:1 molar ratio of total-protein to QD, as described previously.[39] For each sample three TEM images were analysed using MATLAB (MathWorks, 2018b); one of the three images for each mixture is shown in **Figure S6B-G** of Supporting Information. Detected objects were manually checked to eliminate false selection before fitting particle diameter histograms with a lognormal distribution with an upper cut-off of 33 nm, as illustrated in **Figure S15** of Supporting Information.

Measurement and fitting of RC photo-oxidation. Measurements of P870 photo-oxidation were carried out as described previously[39] except the QD concentration was set to 0.1 μM. Samples were incubated in the dark for 5 mins in the presence of a five-fold molar excess of UQ_0 to RC to reconstitute the Q_B site, and then exposed to a 7 s period of illumination (~0.1 mW cm^{-2}). The profile of the excitation light centred at 650 nm was as indicated in **Figure S7A** of Supporting Information. Each measurement was repeated five times and averaged ΔA_{870nm} traces (**Figure S8**, Supporting Information) were fitted to a model assuming a simple interconversion between the ground and photo-oxidised state of P870:

$$P870 \underset{k_r}{\overset{k_f}{\leftrightarrow}} P870^{+} \qquad (\mathbf{1})$$

Modelling of tri-component nanoconjugates. Assembly of tri-component nanoconjugates was modelled as a competitive process in which each protein binds to free “sites”

on the QD surface that are not occluded by already-bound protein. Following the depiction in **Figure 5A**, nanoconjugates formed in protein mixtures with different total-protein:QD and $LHCII_H$:RC_H ratios were modelled using the reaction schemes:

$$RC_{His} + RC_{i-1}LHCII_{j-1}QD \underset{k_{r,RC}(i,j)}{\overset{k_{f,RC}(i,j)}{\rightleftharpoons}} RC_iLHCII_{j-1}QD \quad (\mathbf{2})$$

$$LHCII_{His} + RC_{i-1}LHCII_{j-1}QD \underset{k_{r,LHCII}(i,j)}{\overset{k_{f,LHCII}(i,j)}{\rightleftharpoons}} RC_{i-1}LHCII_jQD \quad (\mathbf{3})$$

where k_f and k_r are macroscopic association and dissociation rate constants, respectively, for each protein at given valences (*i,j*) of the two proteins, and $LHCII_{His}$ and RC_{His} are the total protein population adjusted for any fraction unable to bind (see Sections 2 and 5 of Supporting Information).

The macroscopic association rate constants ($k_{f,RC}$ *and* $k_{f,LHCII}$) in **Eqs. 2** and **3** depend on the availability of free QD surface at which to bind. This availability was parameterised by score matrices of fractional occupation of a QD surface by either RC_H (S_{RC}) or $LHCII_H$ (S_{LHCII}) in tri-component nanoconjugates, that were constructed using:

$$S_{RC}(i,j) = \frac{i}{\bar{n}_{RC}} + \alpha\frac{j}{\bar{n}_{LHCII}} \quad (\mathbf{4})$$

$$S_{LHCII}(i,j) = \beta\frac{i}{\bar{n}_{RC}} + \frac{j}{\bar{n}_{LHCII}} \quad (\mathbf{5})$$

where $\bar{n}_{RC}$ and $\bar{n}_{LHCII}$ were maximum permitted binding valences determined from studies of di-component nanoconjugates (15 and 17, respectively), *i* denoted any possible RC_H:QD valence between 0 and 15 and *j* denoted any possible $LHCII_H$:QD valence between 0 and 17. Parameter α was included in **Eq. 4** to account for the influence of already bound $LHCII_H$ on binding of an additional RC_H and parameter β was included in **Eq. 5** to account for the reverse influence; these were required to account for the experimental observation that binding biased toward RC_H at total-protein:QD ratios >10 (see main text).

Macroscopic association (k_f) and dissociation (k_r) rate constants for RC_H and $LHCII_H$ were deduced from pairs of imaginary microscopic kinetic constants (k_{on}, k_{off}) that were determined from the thermodynamic constants $k_{micro,RC}$ = 8.2 μM^{-1} from previous work[39] and $k_{micro,LHCII}$ = 7.2

μM^{-1} (see Section 2 of Supporting Information), following the relationship $k_{micro} = k_{on}/k_{off}$. Matrices of k_f *and* k_r for each protein were determined from:

$$k_{f,RC}(i,j) = \bar{n}_{RC}(1 - S_{RC}(i,j))k_{on,RC} \quad (6)$$

$$k_{f,LHCII}(i,j) = \bar{n}_{LHCII}(1 - S_{LHCII}(i,j))k_{on,LHCII} \quad (7)$$

$$k_{r,RC}(i,j) = ik_{off,RC} \quad (8)$$

$$k_{r,LHCII}(i,j) = jk_{off,LHCII} \quad (9)$$

where i = 0,1, 2,…, $\bar{n}_{RC}$ and j = 0,1, 2,…, $\bar{n}_{LHCII}$.

The best fit of model to data (**Figure 5B**) was achieved with α = 0.63 and β = 0.78. The S_{RC} or S_{LHCII} score matrices from this best fit are shown in **Figure S16A** of Supporting Information with all values ≤ 1 highlighted in colour. The associated k_f *and* k_r matrices for each protein are shown in **Figure S16B-C** of Supporting Information.

Distributions in the composition of tri-component nanoconjugates were investigated by applying the k_f *and* k_r matrices to ODEs (ordinary differential equations) following **Eqs. 2** and **3** and conducting simulations until equilibria were reached.

Measurements of ET by fluorescence spectroscopy. Titrations of $LHCII_H$ and QD fluorescence were carried out using a Cary Eclipse fluorescence spectrometer (Agilent) and black 96-well microplates (Greiner Bio-One). The QD concentration was fixed at 50 nM and the protein concentration varied, with four repeats. The sample volume was 100 µL in Tris/DDM. Fluorescence spectra were baseline corrected and individual $LHCII_H$ and QD fluorescence components (maxima at 682 nm and 750 nm, respectively) deconvoluted (**Figure S17**, Supporting Information). Intensities at the maximum of the relevant deconvoluted band were used to quantify the fluorescence from $LHCII_H$ in tri-component ($FL_{Tri,LHCII}$; mixture denoted $LHCIII_H/RC_H$/QD) or di-component ($FL_{Di,LHCII}$; mixture denoted RC_{WT} + $LHCIII_H$/QD) nanoconjugates or the fluorescence from QDs in tri-component ($FL_{Tri,QD}$) or di-component ($FL_{Di,QD}$) nanoconjugates. Fluorescence intensities from concentration-matched $LHCII_H$-only or QD-only samples were denoted FL_{LHCII} and FL_{QD}, respectively. $LHCII_H$ or QD fluorescence from a nanoconjugate relative to that from the appropriate concentration-matched sample (R) was determined according to: $R_{Di,LHCII} = FL_{Di,LHCII}/FL_{LHCII}$; $R_{Tri,LHCII} = FL_{Tri,LHCII}/FL_{LHCII}$; $R_{Di,QD} = FL_{Di,QD}/FL_{QD}$ or $R_{Tri,QD} = FL_{Tri,QD}/FL_{QD}$.

Estimation of the efficiencies of direct and indirect ET in tri-component nanoconjugates. E_{Direct} and $E_{Indirect}$ were estimated on the basis of the relative yields of $LHCII_H$ or QD fluorescence from tri-component ($R_{Tri,LHCII}$ or $R_{Tri,QD}$) and di-component ($R_{Di,LHCII}$ or $R_{Di,QD}$) nanoconjugates (see above). Equations used were:

$$E_{Direct} = \frac{F_{Di,LHCII}(1 - R_{Tri,LHCII}) - F_{Tri,LHCII}(1 - R_{Di,LHCII})}{F_{Tri,LHCII}(F_{Di,LHCII} - 1 + R_{Di,LHCII})} \quad (\mathbf{10})$$

$$E_{Indirect} = E'_{LHCIItoQD} E'_{QDtoRC} \quad (\mathbf{11})$$

where $F_{Tri,LHCII}$ and $F_{Di,LHCII}$ were the fraction of $LHCII_H$ in the tri- and di-component nanoconjugates. $E'_{LHCIItoQD}$ and E'_{QDtoRC} were effective ET efficiencies obtained by adjusting measured ET efficiencies $E_{LHCIItoQD}$ and E_{QDtoRC} for the fraction of FRET inactive nanoconjugates. Full details of the derivation and solution of these equations are given in Section 5 of Supporting Information.

Supporting Information

Notes on the design and preparation of His-tagged and native LHCII and RCs; notes on modelling of the thermodynamics of $LHCII_H$/QD conjugate formation; notes on the characterization of energy transfer efficiencies and mechanisms in conjugates; figures S1-S23; supporting references are provided as a single file (.pdf). This material is available free of charge *via* the Internet at http://pubs.acs.org.

Author contributions

J.L and M.R.J conceived the research. J.L. designed constructs, characterised ET in the conjugates and conducted all modelling and thermodynamic analysis. J.L. and J.M. collected TEM data and J.L. carried out the image analysis. J.L and M.R.J drafted the manuscript and all authors commented on the manuscript. M.R.J supervised the project.

Associated content

The authors declare no competing interests.

Acknowledgements

The Lhcb1.3 plasmid was a kind gift from Prof. Roberta Croce from the Vrije Universiteit Amsterdam, The Netherlands. XylE was a kind gift from Dr. Natalie Di Bartolo, University of Bristol.

TEM was carried out at the Wolfson Bioimaging Facility at the University of Bristol. The project was funded by the EPSRC/BBSRC Synthetic Biology Centre for Doctoral Training (EP/L016494/1) and from the BrisSynBio Synthetic Biology Research Centre at the University of Bristol (BB/L01386X/1).

References

(1) Ort, D. R.; Merchant, S. S.; Alric, J.; Barkan, A.; Blankenship, R. E.; Bock, R.; Croce, R.; Hanson, M. R.; Hibberd, J. M.; Long, S. P.; Moore, T. A.; Moroney, J.; Niyogi, K. K.; Parry, M. A. J.; Peralta-Yahya, P. P.; Prince, R. C.; Redding, K. E.; Spalding, M. H.; van Wijk, K. J.; Vermaas, W. F. J.; *et al*. Redesigning Photosynthesis to Sustainably Meet Global Food and Bioenergy Demand. *Proc. Natl. Acad. Sci.* **2015**, *112*, 8529–8536.

(2) Friebe, V. M.; Frese, R. N. Photosynthetic Reaction Center-Based Biophotovoltaics. *Curr. Opin. Electrochem.* **2017**, *5*, 126–134.

(3) McConnell, I.; Li, G.; Brudvig, G. W. Energy Conversion in Natural and Artificial Photosynthesis. *Chem. Biol.* **2010**, *17*, 434–447.

(4) Larkum, A. W. D. Limitations and Prospects of Natural Photosynthesis for Bioenergy Production. *Curr. Opin. Biotechnol.* **2010**, *21*, 271–276.

(5) Blankenship, R. E.; Tiede, D. M.; Barber, J.; Brudvig, G. W.; Fleming, G.; Ghirardi, M.; Gunner, M. R.; Junge, W.; Kramer, D. M.; Melis, A.; Moore, T. A.; Moser, C. C.; Nocera, D. G.; Nozik, A. J.; Ort, D. R.; Parson, W. W.; Prince, R. C.; Sayre, R. T. Comparing Photosynthetic and Photovoltaic Efficiencies and Recognizing the Potential for Improvement. *Science* **2011**, *332*, 805–809.

(6) Stomp, M.; Huisman, J.; Stal, L. J.; Matthijs, H. C. P. Colorful Niches of Phototrophic Microorganisms Shaped by Vibrations of the Water Molecule. *ISME J.* **2007**, *1*, 271–282.

(7) Mirkovic, T.; Ostroumov, E. E.; Anna, J. M.; van Grondelle, R.; Govindjee; Scholes, G. D. Light Absorption and Energy Transfer in the Antenna Complexes of Photosynthetic Organisms. *Chem. Rev.* **2017**, *117*, 249–293.

(8) Saer, R. G.; Blankenship, R. E. Light Harvesting in Phototrophic Bacteria: Structure and Function. *Biochem. J.* **2017**, *474*, 2107–2131.

(9) Scholes, G. D.; Fleming, G. R.; Olaya-Castro, A.; van Grondelle, R. Lessons from Nature about Solar Light Harvesting. *Nat. Chem.* **2011**, *3*, 763–774.

(10) Croce, R.; van Amerongen, H. Natural Strategies for Photosynthetic Light Harvesting. *Nat. Chem. Biol.* **2014**, *10*, 492–501.

(11) Inganäs, O.; Sundström, V. Solar Energy for Electricity and Fuels. *Ambio* **2016**, *45*, S15–

S23.

(12) Badura, A.; Kothe, T.; Schuhmann, W.; Rögner, M. Wiring Photosynthetic Enzymes to Electrodes. *Energy Environ. Sci.* **2011**, *4*, 3263–3274.

(13) Milano, F.; Punzi, A.; Ragni, R.; Trotta, M.; Farinola, G. M. Photonics and Optoelectronics with Bacteria : Making Materials from Photosynthetic Microorganisms. *Adv. Funct. Mater.* **2018**, *1805521*, 1–17.

(14) Ravi, S. K.; Wu, T.; Udayagiri, V. S.; Vu, X. M.; Wang, Y.; Jones, M. R.; Tan, S. C. Photosynthetic Bioelectronic Sensors for Touch Perception, UV-Detection, and Nanopower Generation: Toward Self-Powered E-Skins. *Adv. Mater.* **2018**, *1802290*, 1–9.

(15) Sokol, K. P.; Robinson, W. E.; Warnan, J.; Kornienko, N.; Nowaczyk, M. M.; Ruff, A.; Zhang, J. Z.; Reisner, E. Bias-Free Photoelectrochemical Water Splitting with Photosystem II on a Dye-Sensitized Photoanode Wired to Hydrogenase. *Nat. Energy* **2018**, *3*, 944–951.

(16) Kornienko, N.; Zhang, J. Z.; Sakimoto, K. K.; Yang, P.; Reisner, E. Interfacing Nature's Catalytic Machinery with Synthetic Materials for Semi-Artificial Photosynthesis. *Nat. Nanotechnol.* **2018**, *13*, 890–899.

(17) Boghossian, A. A.; Ham, M.-H.; Choi, J. H.; Strano, M. S. Biomimetic Strategies for Solar Energy Conversion: A Technical Perspective. *Energy Environ. Sci.* **2011**, *4*, 3834–3843.

(18) Kim, Y.; Shin, S. A.; Lee, J.; Yang, K. D.; Nam, K. T. Hybrid System of Semiconductor and Photosynthetic Protein. *Nanotechnology* **2014**, *25*, 1–20.

(19) Yehezkeli, O.; Tel-Vered, R.; Michaeli, D.; Willner, I.; Nechushtai, R. Photosynthetic Reaction Center-Functionalized Electrodes for Photo-Bioelectrochemical Cells. *Photosynth. Res.* **2014**, *120*, 71–85.

(20) Operamolla, A.; Ragni, R.; Milano, F.; Tangorra, R. R.; Antonucci, A.; Agostiano, A.; Trotta, M.; Farinola, G. "Garnishing" the Photosynthetic Bacterial Reaction Center for Bioelectronics. *J. Mater. Chem. C* **2015**, *3*, 6471–6478.

(21) Fukuzumi, S.; Lee, Y.-M.; Nam, W. Mimicry and Functions of Photosynthetic Reaction Centers. *Biochem. Soc. Trans.* **2018**, *46*, 1279–1288.

(22) Wang, F.; Liu, X.; Willner, I. Integration of Photoswitchable Proteins, Photosynthetic Reaction Centers and Semiconductor/Biomolecule Hybrids with Electrode Supports for Optobioelectronic Applications. *Adv. Mater.* **2013**, *25*, 349–377.

(23) Nguyen, K.; Bruce, B. D. Growing Green Electricity: Progress and Strategies for Use of Photosystem I for Sustainable Photovoltaic Energy Conversion. *Biochim. Biophys. Acta - Bioenerg.* **2014**, *1837*, 1553–1566.

(24) Ravi, S. K.; Tan, S. C. Progress and Perspectives in Exploiting Photosynthetic Biomolecules for Solar Energy Harnessing. *Energy Environ. Sci.* **2015**, *8*, 2551–2573.

(25) Ham, M.-H.; Choi, J. H.; Boghossian, A. A.; Jeng, E. S.; Graff, R. A.; Heller, D. A.; Chang, A. C.; Mattis, A.; Bayburt, T. H.; Grinkova, Y. V; Zeiger, A. S.; Van Vliet, K. J.; Hobbie, E. K.; Sligar, S. G.; Wraight, C. A.; Strano, M. S. Photoelectrochemical Complexes for Solar Energy Conversion That Chemically and Autonomously Regenerate. *Nat. Chem.* **2010**, *2*, 929–936.

(26) Suresh, L.; Vaghasiya, J. V; Nandakumar, D. K.; Wu, T.; Jones, M. R.; Tan, S. C. High-Performance UV Enhancer Molecules Coupled with Photosynthetic Proteins for Ultra-Low-Intensity UV Detection. *Chem* **2019**, *5*, 1847–1860.

(27) Friebe, V. M.; Delgado, J. D.; Swainsbury, D. J. K.; Gruber, J. M.; Chanaewa, A.; Van Grondelle, R.; Von Hauff, E.; Millo, D.; Jones, M. R.; Frese, R. N. Plasmon-Enhanced Photocurrent of Photosynthetic Pigment Proteins on Nanoporous Silver. *Adv. Funct. Mater.* **2016**, *26*, 285–292.

(28) Ravi, S. K.; Yu, Z.; Swainsbury, D. J. K.; Ouyang, J.; Jones, M. R.; Tan, S. C. Enhanced Output from Biohybrid Photoelectrochemical Transparent Tandem Cells Integrating Photosynthetic Proteins Genetically Modified for Expanded Solar Energy Harvesting. *Adv. Energy Mater.* **2017**, *7*, 1–7.

(29) Zhang, H.; Carey, A.-M.; Jeon, K.-W.; Liu, M.; Murrell, T. D.; Locsin, J.; Lin, S.; Yan, H.; Woodbury, N.; Seo, D.-K. A Highly Stable and Scalable Photosynthetic Reaction Center–Graphene Hybrid Electrode System for Biomimetic Solar Energy Transduction. *J. Mater. Chem. A* **2017**, *5*, 6038–6041.

(30) Friebe, V. M.; Millo, D.; Swainsbury, D.; Jones, M. R.; Frese, R. N. Cytochrome c Provides an Electron-Funneling Antenna for Efficient Photocurrent Generation in a Reaction Center Biophotocathode. *ACS Appl. Mater. Interfaces* **2017**, *9*, 23379–23388.

(31) Ravi, S. K.; Swainsbury, D. J. K.; Singh, V. K.; Ngeow, Y. K.; Jones, M. R.; Tan, S. C. A Mechanoresponsive Phase-Changing Electrolyte Enables Fabrication of High-Output Solid-State Photobioelectrochemical Devices from Pigment-Protein Multilayers. *Adv. Mater.* **2018**, *30*, 1–8.

(32) Singh, V. K.; Ravi, S. K.; Ho, J. W.; Wong, J. K. C.; Jones, M. R.; Tan, S. C. Biohybrid Photoprotein-Semiconductor Cells with Deep-Lying Redox Shuttles Achieve a 0.7 V Photovoltage. *Adv. Funct. Mater.* **2018**, *28*, 1703689.

(33) Noji, T.; Matsuo, M.; Takeda, N.; Sumino, A.; Kondo, M.; Nango, M.; Itoh, S.; Dewa, T. Lipid-Controlled Stabilization of Charge-Separated States ($P^+Q_B^-$) and Photocurrent

Generation Activity of a Light-Harvesting–Reaction Center Core Complex (LH1-RC) from Rhodopseudomonas Palustris. *J. Phys. Chem. B* **2018**, *122*, 1066–1080.

(34) Ravi, S. K.; Rawding, P.; Elshahawy, A. M.; Huang, K.; Sun, W.; Zhao, F.; Wang, J.; Jones, M. R.; Tan, S. C. Photosynthetic Apparatus of *Rhodobacter sphaeroides* Exhibits Prolonged Charge Storage. *Nat. Commun.* **2019**, *10*, 902.

(35) Werwie, M.; Xu, X.; Haase, M.; Basche, T.; Paulsen, H. Bio Serves Nano : Biological Light-Harvesting Complex as Energy Donor for Semiconductor Quantum Dots. *Langmuir* **2012**, *28*, 5810–5818.

(36) Gundlach, K.; Werwie, M.; Wiegand, S.; Paulsen, H. Filling the “Green Gap” of the Major Light-Harvesting Chlorophyll A/B Complex by Covalent Attachment of Rhodamine Red. *Biochim. Biophys. Acta - Bioenerg.* **2009**, *1787*, 1499–1504.

(37) Dutta, P. K.; Lin, S.; Loskutov, A.; Levenberg, S.; Jun, D.; Saer, R.; Beatty, J. T.; Liu, Y.; Yan, H.; Woodbury, N. W. Reengineering the Optical Absorption Cross-Section of Photosynthetic Reaction Centers. *J. Am. Chem. Soc.* **2014**, *136*, 4599–4604.

(38) Yoneda, Y.; Noji, T.; Katayama, T.; Mizutani, N.; Komori, D.; Nango, M.; Miyasaka, H.; Itoh, S.; Nagasawa, Y.; Dewa, T. Extension of Light-Harvesting Ability of Photosynthetic Light-Harvesting Complex 2 (LH2) through Ultrafast Energy Transfer from Covalently Attached Artificial Chromophores. *J. Am. Chem. Soc.* **2015**, *137*, 13121–13129.

(39) Liu, J.; Mantell, J.; Di Bartolo, N.; Jones, M. R. Mechanisms of Self-Assembly and Energy Harvesting in Tuneable Conjugates of Quantum Dots and Engineered Photovoltaic Proteins. *Small* **2019**, *15*, 1804267.

(40) Nagakawa, H.; Takeuchi, A.; Takekuma, Y.; Noji, T.; Kawakami, K.; Kamiya, N.; Nango, M.; Furukawa, R.; Nagata, M. Efficient Hydrogen Production Using Photosystem I Enhanced by Artificial Light Harvesting Dye. *Photochem. Photobiol. Sci.* **2019**, *18*, 309–313.

(41) Werwie, M.; Dworak, L.; Bottin, A.; Mayer, L.; Basché, T.; Wachtveitl, J.; Paulsen, H. Light-Harvesting Chlorophyll Protein (LHCII) Drives Electron Transfer in Semiconductor Nanocrystals. *BBA - Bioenerg.* **2018**, *1859*, 174–181.

(42) Efros, A. L.; Rosen, M. The Electronic Structure of Semiconductor Nanocrystals. *Annu. Rev. Mater. Sci.* **2000**, *30*, 475–521.

(43) Natali, A.; Roy, L. M.; Croce, R. *In Vitro* Reconstitution of Light-Harvesting Complexes of Plants and Green Algae. *J. Vis. Exp.* **2014**, *92*, 1–13.

(44) Tachiya, M. Kinetics of Quenching of Luminescent Probes in Micellar Systems. II. *J. Chem. Phys.* **1982**, *76*, 340–348.

(45) Martinez, J. C.; Murciano-Calles, J.; Cobos, E. S.; Iglesias-Bexiga, M.; Luque, I.; Ruiz-Sanz, J.; Murciano Calles, J.; Cobos, E. S.; Iglesias Bexiga, M.; Luque, I.; Ruiz Sanz, J. Isothermal Titration Calorimetry : Thermodynamic Analysis of the Binding Thermograms of Molecular Recognition Events by Using Equilibrium Models. In *Applications of Calorimetry in a Wide Context*; Cobos, E. S., Elkordy, A. A., Eds.; InTech: London, 2013; pp 73–104.

(46) Pons, T.; Medintz, I. I. L.; Wang, X.; English, D. S.; Mattoussi, H. Solution-Phase Single Quantum Dot Fluorescence Resonance Energy Transfer. *J. Am. Chem. Soc.* **2006**, *128*, 15324–15331.

(47) Aldeek, F.; Safi, M.; Zhan, N.; Palui, G.; Mattoussi, H. Understanding the Self-Assembly of Proteins onto Gold Nanoparticles and Quantum Dots Driven by Metal-Histidine Coordination. *ACS Nano* **2013**, *7*, 10197–10210.

(48) Werwie, M.; Fehr, N.; Xu, X.; Basché, T.; Paulsen, H. Comparison of Quantum Dot-Binding Protein Tags: Affinity Determination by Ultracentrifugation and FRET. *Biochim. Biophys. Acta - Gen. Subj.* **2014**, *1840*, 1651–1656.

(49) Liu, J.; Friebe, V. M.; Swainsbury, D.; Crouch, L. I.; Szabo, D.; Frese, R. N.; Jones, M. Engineered Photoproteins That Give Rise to Photosynthetically-Incompetent Bacteria Are Effective as Photovoltaic Materials for Biohybrid Photoelectrochemical Cells. *Faraday Discuss.* **2018**, *207*, 307–327.

(50) Wei, X.; Su, X.; Cao, P.; Liu, X.; Chang, W.; Li, M.; Zhang, X.; Liu, Z. Structure of Spinach Photosystem II-LHCII Supercomplex at 3.2 Å Resolution. *Nature* **2016**, *534*, 69–74.

(51) Su, X.; Wei, X.; Zhu, D.; Chang, W.; Liu, Z. Structure and Assembly Mechanism of Plant $C_2S_2M_2$-Type PSII-LHCII Supercomplex. *Science* **2017**, *820*, 815–820.

(52) Dall'Osto, L.; Ünlü, C.; Cazzaniga, S.; van Amerongen, H. Disturbed Excitation Energy Transfer in *Arabidopsis Thaliana* Mutants Lacking Minor Antenna Complexes of Photosystem II. *Biochim. Biophys. Acta - Bioenerg.* **2014**, *1837*, 1981–1988.

(53) Hohmann-Marriott, M. F.; Blankenship, R. E. Evolution of Photosynthesis. *Annu Rev Plant Biol* **2011**, *62*, 515–548.

(54) Björkman, O.; Demmig, B. Photon Yield of O_2 Evolution and Chlorophyll Fluorescence Characteristics at 77 K among Vascular Plants of Diverse Origins. *Planta.* **1987**, *170*, 489–504.

(55) Timpmann, K.; Chenchiliyan, M.; Jalviste, E.; Timney, J. A.; Hunter, C. N.; Freiberg, A. Efficiency of Light Harvesting in a Photosynthetic Bacterium Adapted to Different Levels of Light. *BBA - Bioenerg.* **2014**, *1837*, 1835–1846.

(56) Wientjes, E.; van Amerongen, H.; Croce, R. Quantum Yield of Charge Separation in Photosystem II: Functional Effect of Changes in the Antenna Size upon Light Acclimation. *J. Phys. Chem. B* **2013**, *117*, 11200–11208.

(57) Mascoli, V.; Novoderezhkin, V.; Liguori, N.; Xu, P.; Croce, R. Design Principles of Solar Light Harvesting in Plants : Functional Architecture of the Monomeric Antenna CP29. *BBA - Bioenerg.* **2020**, *1861*, 148156.

(58) Wientjes, E.; van Amerongen, H.; Croce, R. LHCII Is an Antenna of Both Photosystems after Long-Term Acclimation. *Biochim. Biophys. Acta - Bioenerg.* **2013**, *1827*, 420–426.

(59) Swainsbury, D. J. K.; Friebe, V. M.; Frese, R. N.; Jones, M. R. Evaluation of a Biohybrid Photoelectrochemical Cell Employing the Purple Bacterial Reaction Centre as a Biosensor for Herbicides. *Biosens. Bioelectron.* **2014**, *58*, 172–178.

(60) Krüger, T. P. J.; Novoderezhkin, V. I.; Ilioaia, C.; van Grondelle, R. Fluorescence Spectral Dynamics of Single LHCII Trimers. *Biophys. J.* **2010**, *98*, 3093–3101.

Figures

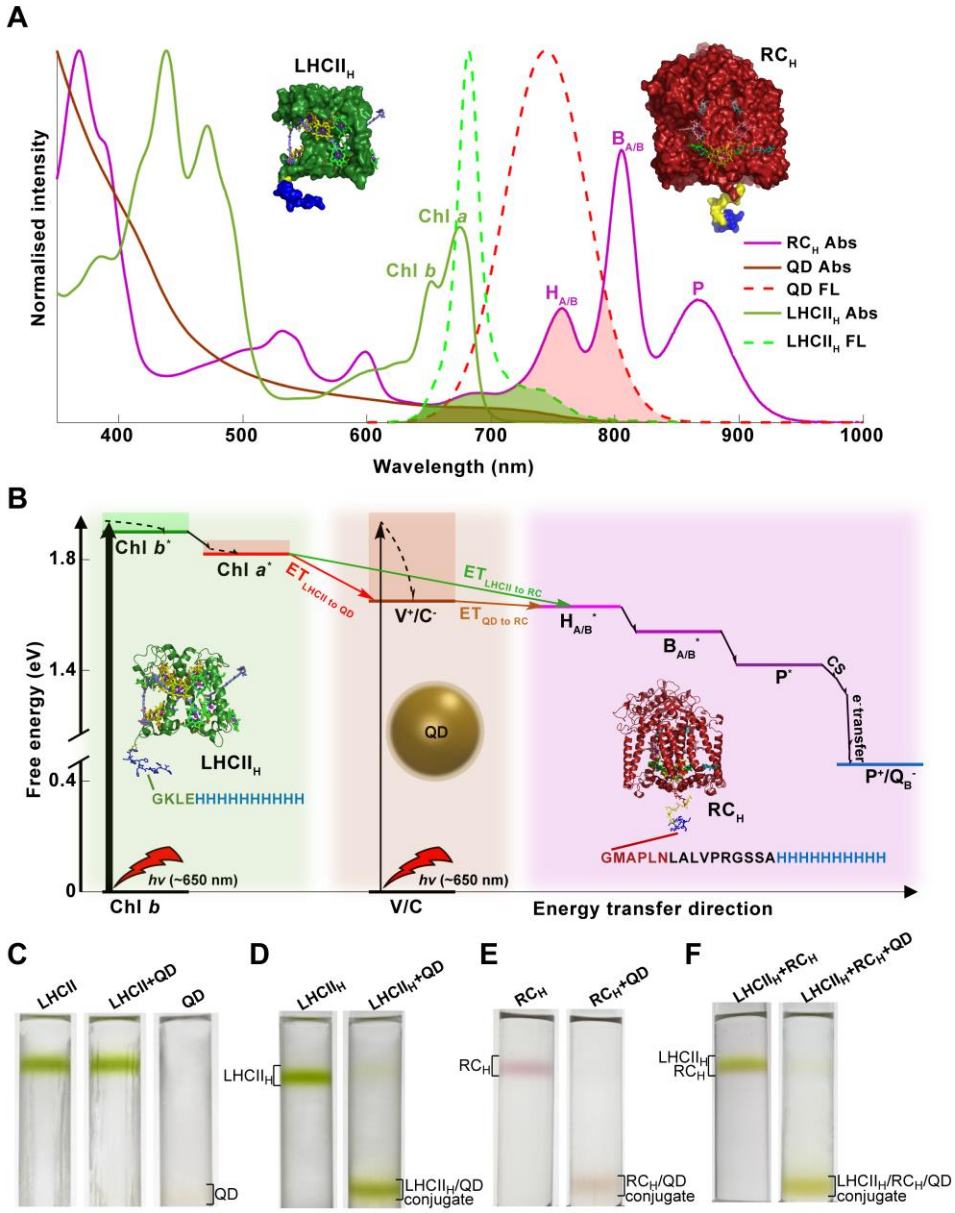

Figure 1. Design and formation of protein/QD nanoconjugates. (A) Normalised absorbance and fluorescence spectra of components. Spectral overlap between $LHCII_H$ fluorescence and RC_H absorbance (9.34×10^{-13} cm^{-3}) is shown in light green shadow, that between $LHCII_H$ fluorescence and QD absorbance (3.77×10^{-12} cm^{-3}) in green/brown shadow, and that between QD fluorescence and RC_H absorbance (3.78×10^{-12} cm^{-3}) in red/green shadow. **(B)** Plot of the envisaged ET scheme in a tri-component conjugate. Light at 650 nm mostly excites mostly Chl *b* in $LHCII_H$, with subsequent relaxation to the red-most Chl *a* cluster.[60] Further energy transfer to the RC can take either a direct pathway (green arrow) or indirect pathway *via* the QD (red/brown

arrows), triggering internal RC energy transfer followed by charge separation (CS). Illumination at 650 nm can also excite the QD or RC directly, but to a much lower extent than LHCII due to their much weaker absorption at this wavelength. For $LHCII_H$ the His_{10}-tag (blue letters) is attached directly to the protein's C-terminus (green letters), while in RC_H a linker (black letters) connects the His_{10}-tag (blue letters) to the C-terminus of the PufM polypeptide (wine letters). **Figure S1** of Supporting Information shows protein structures in more detail**. (C-F**) Two step sucrose density gradients of **C** - spinach LHCII, **D** - $LHCII_H$, **E** - RC_H and **F** - a 1:1 $LHCII_H$:RC_H mix, all in the absence and presence of QDs (10:1 molar ratio of total-protein:QD). Proteins modified with a His_{10}-tag bound to a QD and migrated to the lower (25%/60%) interface in the gradient whilst proteins not bound to a QD remained at the upper (0%/25%) interface.

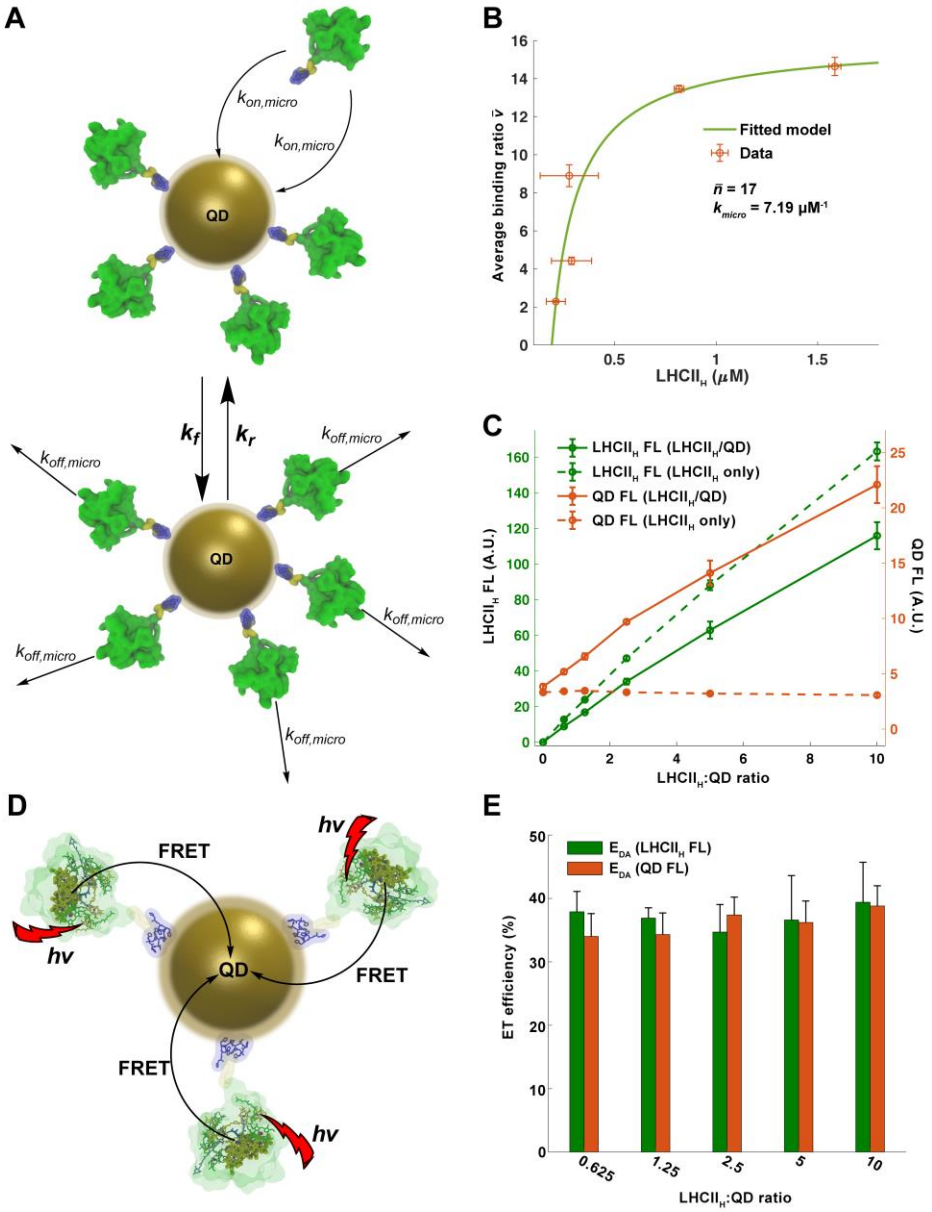

Figure 2. Assembly and ET in LHCII$_H$/QD nanoconjugates. (**A**) Scheme for the interaction between multiple LHCII$_H$ and a QD. Microscopic constants $k_{on,micro}$ and $k_{off,micro}$ describe association/dissociation events between a single LHCII$_H$ and the QD. Parameters k_f and k_r indicate the macroscopic kinetic outcomes that are the consequence of all possible microscopic events (see Section 2 of Supporting Information, **Eqs. S3**-**S5**). (**B**) Fit using **Eq. S1** (Supporting Information) of experimental data on average binding ratio as a function of the concentration of unbound LHCII$_H$. (**C**) Intensity of deconvoluted LHCII$_H$ and QD fluorescence as a function of LHCII$_H$:QD ratio in mixtures (solid-lines), or in concentration-matched LHCII$_H$-only or QD-only samples (dashed-lines). Excitation was at 650 nm. [QD] was held constant at 50 nM and [LHCII$_H$] was varied. Decreased LHCII$_H$ fluorescence and increased QD fluorescence in nanoconjugates

relative to single component controls indicated $LHCII_H$→QD FRET. (**D**) FRET scheme between multiple bound $LHCII_H$ and a QD. Clusters of three low energy Chl *a*, likely the FRET donor, are highlighted in spheres. Due to the QD's ability to accommodate multiple $LHCII_H$ harvesters, QD fluorescence in response to 650 nm excitation increased to nearly six-fold that of a QD-only control at an $LHCII_H$:QD of 10:1. (**E**) Estimates of the efficiency of single donor-single acceptor ET in nanoconjugates formed in mixes with different $LHCII_H$:QD ratios (see Section 3 of Supporting Information).

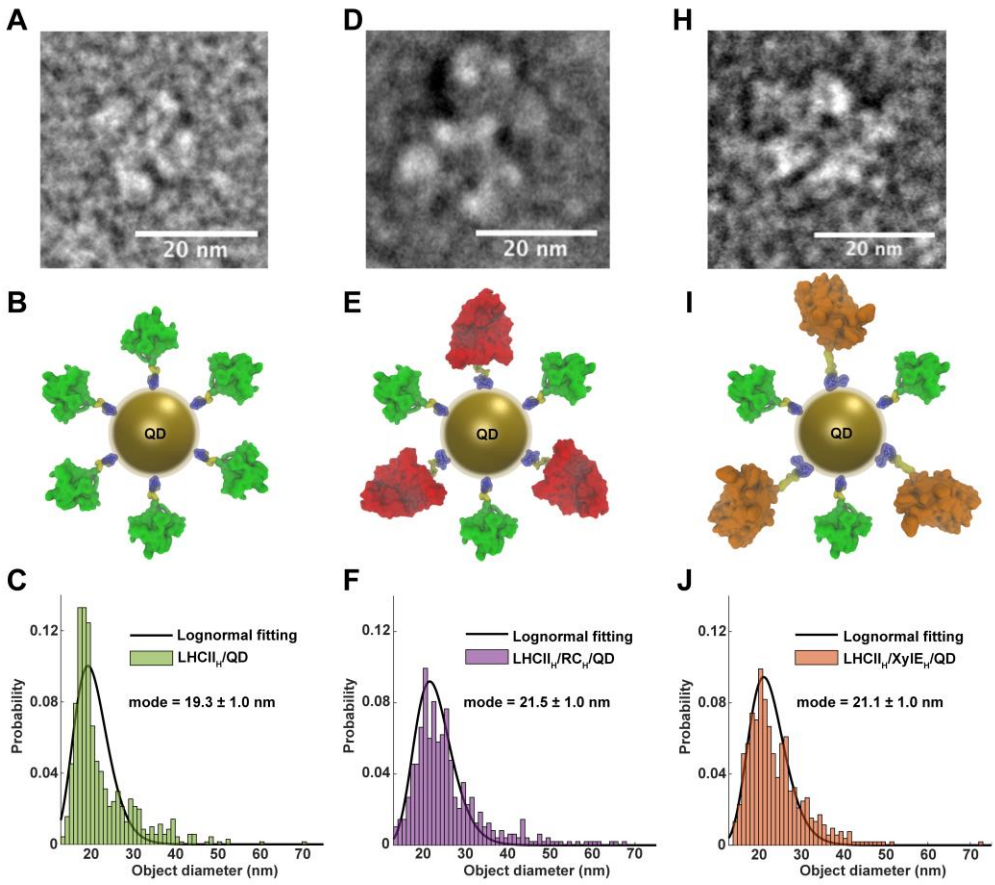

Figure 3. Architectures of protein/QD nanoconjugates. (**A**) An individual $LHCII_H$/QD nanoconjugate from a 10:1 molar mix imaged by TEM. (**B**) Schematic of a $LHCII_H$/QD nanoconjugate with $LHCII_H$ shown with a green surface, C-terminal residues in yellow and the His-tag in blue. (**C**) Histogram of diameters of $LHCII_H$/QD nanoconjugates determined from image analysis (707 objects analysed), and a fitted lognormal distribution. (**D-F**) Equivalent data for $LHCII_H/RC_H$/QD tri-component nanoconjugates from a 5:5:1 molar mix (506 objects analysed), RC_H shown with a red surface, flexible linkers in yellow and the His-tag in blue. (**G-I**) Equivalent data for $LHCII_H/XylE_H$/QD tri-component nanoconjugates from a 5:5:1 molar mix (599 objects analysed). $XylE_H$ shown with an orange surface.

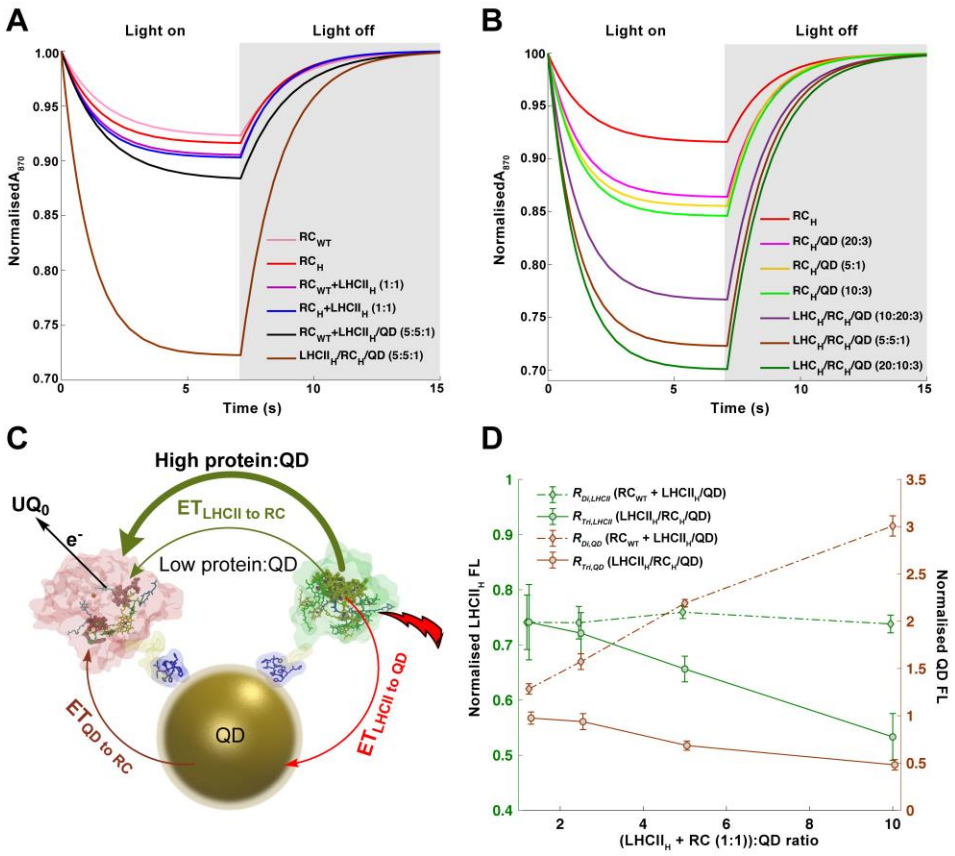

Figure 4. ET and charge separation in $LHCII_H/RC_H/QD$ nanoconjugates. (**A**) Normalised RC photobleaching at 870 nm in mixes with native (RC_{WT}) or His_{10}-tag (RC_H) complexes. Some enhancements of baseline RC photobleaching seen with combinations other than $LHCII_H/RC_H/QD$ are likely to be due to reabsorption of $LHCII_H$ or QD fluorescence. (**B**) Normalised RC_H photobleaching at 870 nm in RC_H/QD or $LHCII_H/RC_H/QD$ nanoconjugates with different compositions. For **A** and **B** excitation was at 650 nm for 7 seconds and data shown are fits to normalised kinetic traces (shown in **Figure S8**, Supporting Information). (**C**) Schematic of a $LHCII_H/RC_H/QD$ nanoconjugate with routes of direct and indirect FRET. Clusters of three low energy Chl *a* in $LHCII_H$ and the RC_H bacteriopheophytins, likely responsible for FRET as donors and acceptors, are highlighted in spheres. The extent of direct FRET should depend on the crowdedness of the protein shell. (**D**) Normalised $LHCII_H$ or QD fluorescence as a function of the ratio of total-protein:QD (with $LHCII_H$:RC_H = 1:1) for $LHCII_H/RC_H/QD$ nanoconjugates or a composition-matched mixture of RC_{WT} and $LHCII_H/QD$ nanoconjugates. After deconvolution, $LHCII_H$ or QD fluorescence was normalised relative to the fluorescence from an equivalent concentration of $LHCII_H$ or QD in single component samples.

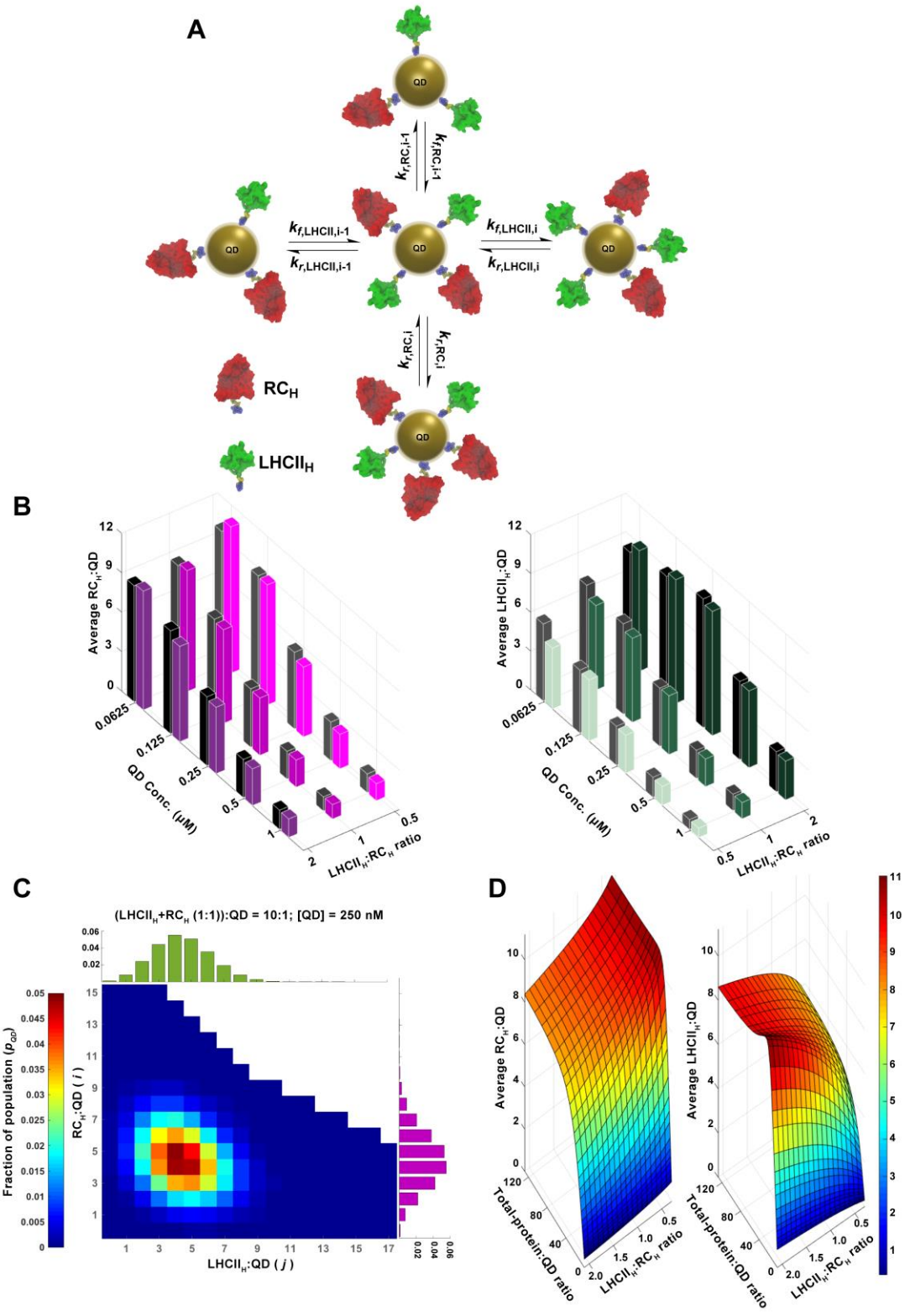

Figure 5. Modelling of $LHCII_H$/RC_H/QD nanoconjugate assembly and composition. (**A**) Scheme for association/dissociation of RC_H (red) and $LHCII_H$ (green) with the surface of a QD as described by **Eqs. 2**,**3**. **(B**) Comparison of data (colour) with the best-fit simulation (black), for the

average RC_H:QD (left) and $LHCII_H$:QD (right) composition of nanoconjugates formed in mixes with five total-protein:QD ratios (achieved by varying [QD]) and three different $LHCII_H$:RC_H ratios. (**C**) Computed population distribution for nanoconjugates formed in a 5:5:1 mix of RC_H, $LHCII_H$ and QDs. Individual distributions of $LHCII_H$:QD and RC_H:QD are shown with green and purple bars, respectively. (**D**) Continuous plots of modelled average RC_H:QD (left) and $LHCII_H$:QD (right) in nanoconjugates as a function of total-protein:QD ratio between 0.625 to 128, and for $LHCII_H$:RC_H ratios between 0.3 and 2.2. Each data point was the average RC_H:QD or $LHCII_H$:QD ratio achieved by summing all bound RC_H or $LHCII_H$ per QD obtained from simulation as shown in **C**.

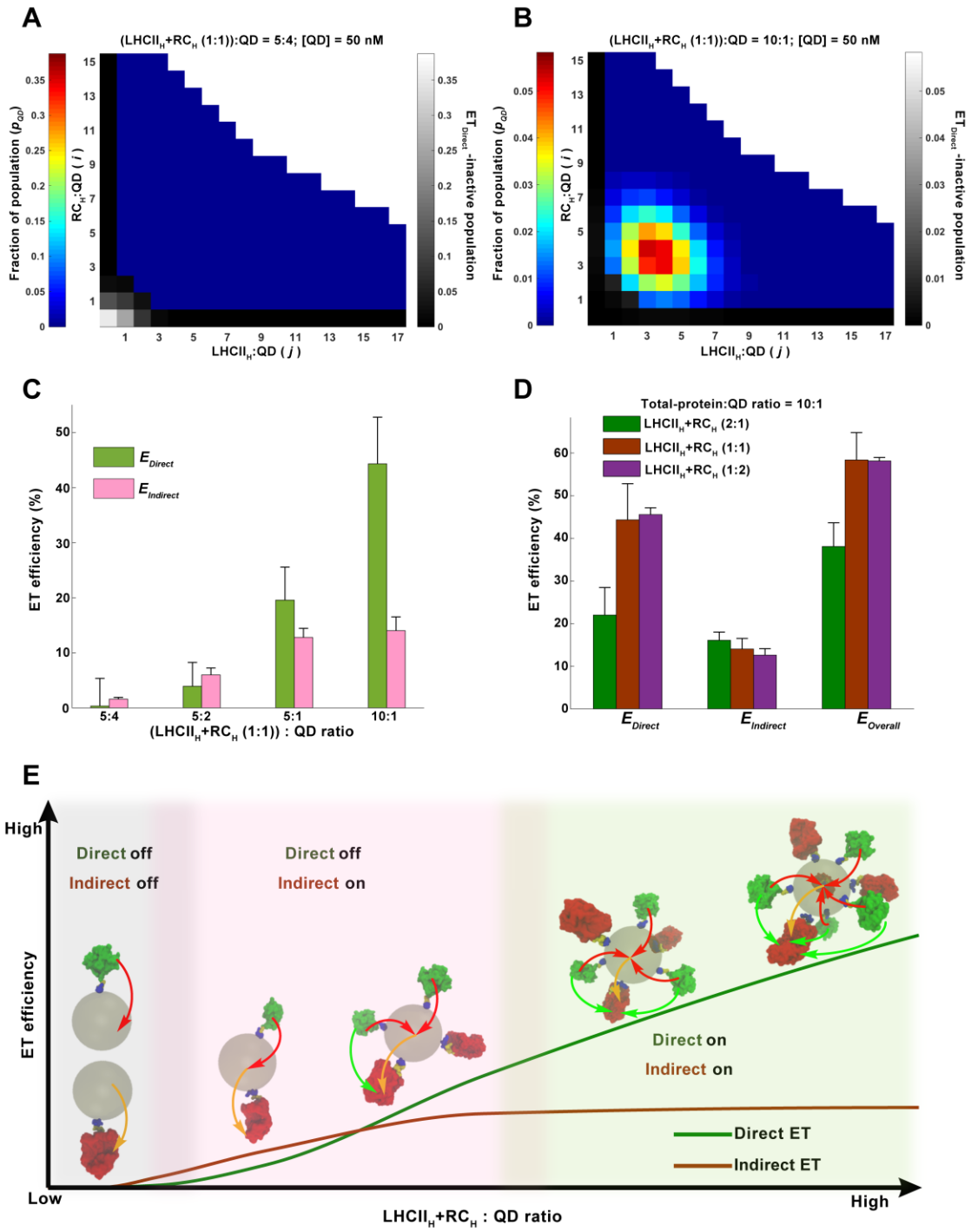

Figure 6. Extents and routes of ET in LHCII$_H$/RC$_H$/QD nanoconjugates. (A-B) Simulated nanoconjugate compositions in mixes with a total-protein:QD ratio of **A** - 5:4 and **B** - 10:1. Compositions that are inactive for FRET are shown in greyscale and include all nanoconjugates where the number of RC$_H$ or LHCII$_H$ bound to a QD is zero (left column and bottom row). (**C**) Efficiencies of direct and indirect LHCII$_H$→RC$_H$ ET in nanoconjugates formed in mixtures with an

equal $LHCII_H$:RC_H ratio and four total-protein:QD ratios. (**D**) Efficiencies of direct, indirect and overall $LHCII_H \rightarrow RC_H$ ET in nanoconjugates with different $LHCII_H$:RC_H ratios at a total-protein:QD = 10:1. $E_{Overall}$ is the sum of E_{Direct} and $E_{Indirect}$. (**E**) Continuous plots of E_{Direct} and $E_{Indirect}$ against total-protein:QD ratio from 0 (low) to 10 (high). Energy flow to one RC_H is shown to illustrate the effect of increasing protein loading. Grey shading indicates the $LHCII_H \rightarrow RC_H$ ET-inactive region at very low total-protein:QD ratio. Pink shading indicates the region in which indirect ET switches on and direct ET starts as the protein load increases. Green shading indicates the region at higher total-protein:QD ratio where direct ET strongly surpasses the indirect route. Green arrows - direct ET; red arrows - $LHCII_H \rightarrow$QD ET; orange arrows - QD$\rightarrow RC_H$ ET.

ToC image